Supporting Information

Breaking the symmetry dependency of symmetry-protected bound states in the continuum via metasurface

Xin Luo (罗欣)[1,2,4], Fei Zhang (张飞)[1,3,4], Mingbo Pu (蒲明博)[1,3,4], Yingli Ha (哈颖丽)[1,3,4], Shilin Yu (余世林)[1,3], Hanlin Bao (包汉霖)[1,4], Qiong He (何琼)[1,3], Ping Gao (高平)[1], Yinghui Guo (郭迎辉)[1,3,4], Mingfeng Xu (徐明峰)[1,3,4], and Xiangang Luo (罗先刚)[1,4*]

[1]Institute of Optics and Electronics, Chinese Academy of Sciences, Chengdu 610209, China

[2]School of Automation Engineering, University of Electronic Science and Technology of China, Chengdu 610054, China

[3]National Key Laboratory of Optical Field Manipulation Science and Technology, Chinese Academy of Sciences, Chengdu 610209, China

[4]College of Materials Science and Opto-Electronic Technology, University of Chinese Academy of Sciences, Beijing 100049, China

[*]lxg@ioe.ac.cn

Section S1: Fano fitting of the quasi-BIC resonances

Here, the Q-factors of the MR, TR, λ_2', λ_1', λ_4', and λ_3' resonances are calculated by fitting the transmission spectrum with the Fano formula[1, 2], as follows:

$$I \propto \frac{(F\gamma + \omega - \omega_0)^2}{(\omega - \omega_0)^2 + \gamma^2} \qquad \text{(S1.1)}$$

Where I is the transmission, F is the Fano parameter, and γ and ω_0 represent the half-full bandwidth and wavelength of the resonance, respectively. Therefore, Q = ω_0 / γ. The fitting results of the MR, TR, λ_2', λ_1', λ_4', and λ_3' resonances are shown in Figs. S1(a)-(f). Here, Δs = 20 nm and ΔL = 40 nm. The Q-factors of the MR, TR, λ_2', λ_1', λ_4', and λ_3' resonances are 605, 697, 57531, 292, 5108, and 1496746, respectively.

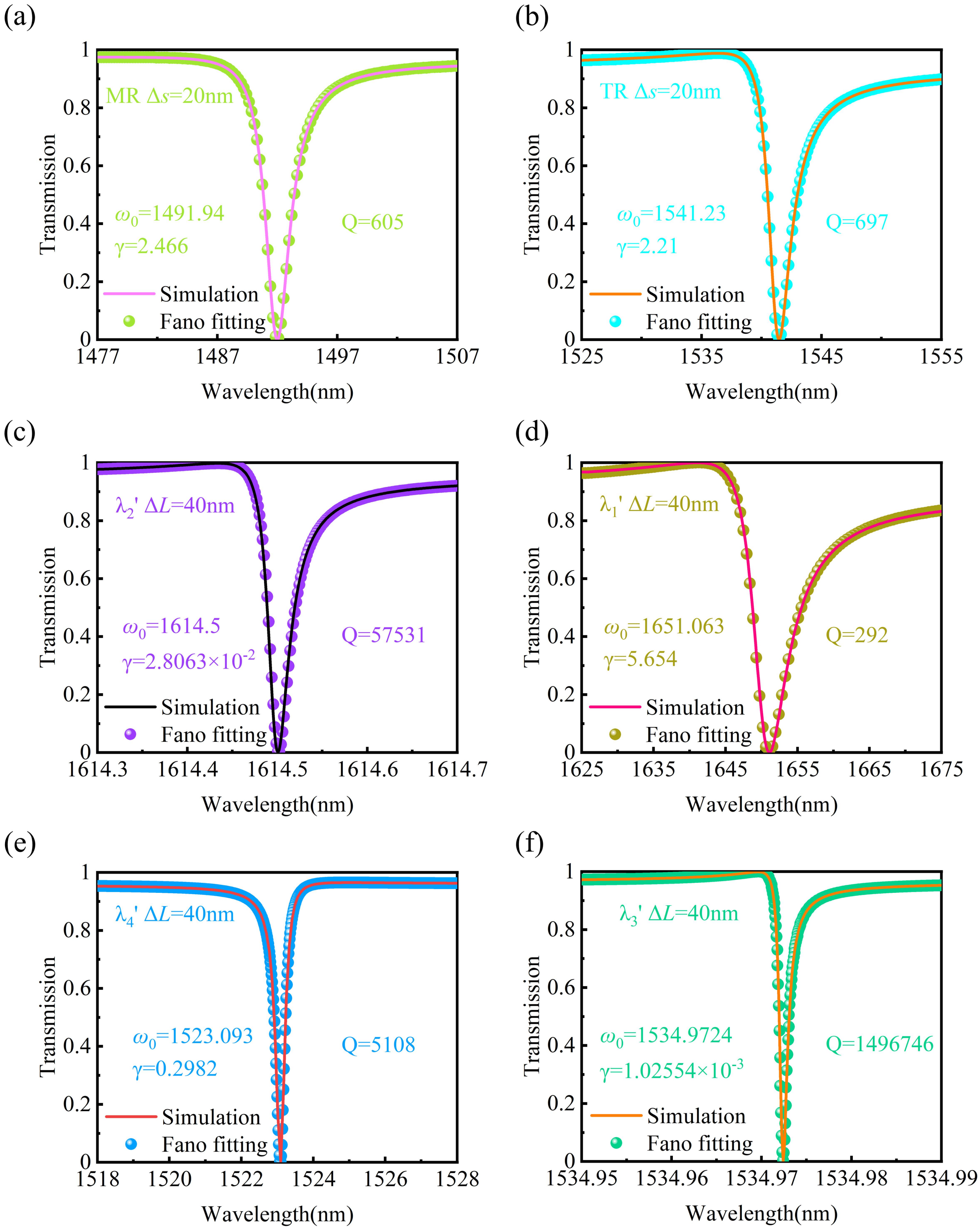

Figure S1. (a)-(f) The Fano fittings of the MR, TR, λ_2', λ_1', λ_4', and λ_3' resonances. The solid lines are simulated results, and the dotted lines are the Fano fittings. The marked Q-factor values are estimated by ω_0 / γ.

Section S2: Multipole decompositions

To better understand the microscopic nature of the excited resonances, we use multipole decomposition calculations in Cartesian coordinates to obtain multipole scattered power contributions[3-7]. According to the induced volume displacement current density J in the unit cell of the metasurface, the electric dipole (P) moment, magnetic dipole (M) moment, electric toroidal dipole (ET) moment, magnetic toroidal dipole (MT) moment, electric quadrupole (Qe) moment, and magnetic quadrupole (Qm) moment can be defined as:

$$P = \frac{1}{i\omega}\int J \, d^3r \qquad \text{(S2.1)}$$

$$M = \frac{1}{2c}\int (r \times J) \, d^3r \qquad \text{(S2.2)}$$

$$ET = \frac{1}{2}\int (r \times P) \, d^3r \qquad \text{(S2.3)}$$

$$MT = \frac{1}{10c}\int [(r \cdot J)r - 2r^2 J] \, d^3r \qquad \text{(S2.4)}$$

$$Qe_{\alpha\beta} = \frac{1}{i\omega}\int [r_\alpha J_\beta + r_\beta J_\alpha - \frac{2}{3}(r \cdot J)] \, d^3r \qquad \text{(S2.5)}$$

$$Qm_{\alpha\beta} = \frac{1}{3c}\int [(r \times J)_\alpha r_\beta + (r \times J)_\beta r_\alpha] \, d^3r \qquad \text{(S2.6)}$$

where c is the speed of light in the vacuum, r is the distance vector from the origin to point (x, y, z) in a Cartesian coordinate system, and α, $\beta = x, y, z$. Therefore, the decomposed far-field scattered powers by these multipole moments can be calculated by using the following equations:

$$I_P = \frac{2\omega^4}{3c^3}|P|^2 \qquad \text{(S2.7)}$$

$$I_M = \frac{2\omega^4}{3c^3}|M|^2 \qquad \text{(S2.8)}$$

$$I_{ET} = \frac{2\omega^6}{3c^5}|ET|^2 \qquad \text{(S2.9)}$$

$$I_{MT} = \frac{2\omega^6}{3c^5}|MT|^2 \qquad \text{(S2.10)}$$

$$I_{Qe} = \frac{\omega^6}{5c^5}\sum|Q_{\alpha\beta}|^2 \qquad \text{(S2.11)}$$

$$I_{Qm} = \frac{\omega^6}{40c^5}\sum|M_{\alpha\beta}|^2 \qquad \text{(S2.12)}$$

The total electromagnetic scattered power can be expressed as:

$$Total = I_P + I_M + I_{ET} + I_{MT} + I_{Qe} + I_{Qm} \qquad \text{(S2.13)}$$

Section S3: Scattered powers of the MR and TR resonance: *x*, *y*, *z* components corresponding to the dominant multipole

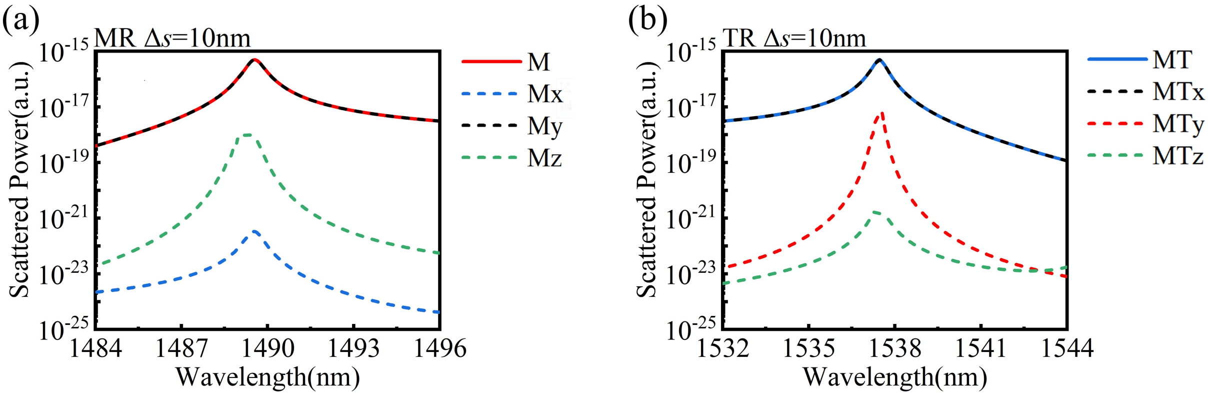

Figure S2. (a)-(b): Scattered powers of the MR and TR resonances: *x*, *y*, and *z* components corresponding to the M and MT, respectively.

Section S4: Scattered powers of the λ₁' (Δ*L*=1nm), λ₂' (Δ*L*=1nm), and λ₁' (Δ*L*=40nm) resonances: *x*, *y*, and *z* components of the M

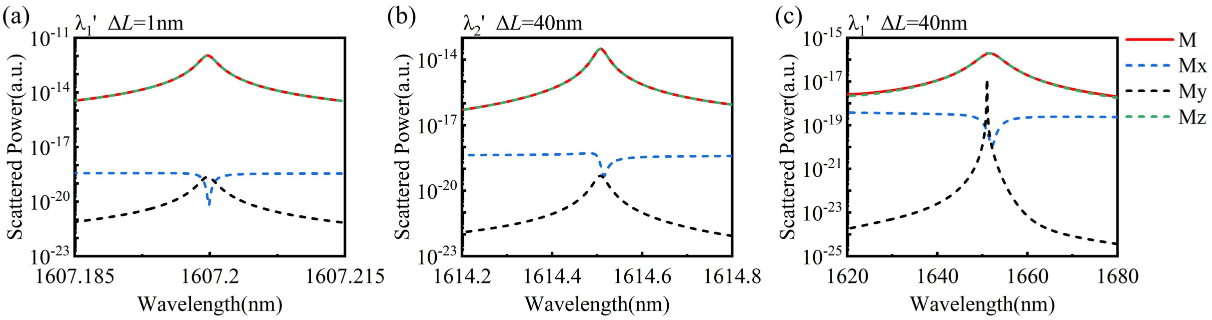

Figure S3. (a)-(b): Scattered powers of the λ_1' (ΔL=1nm), λ_2' (ΔL=1nm), and λ_1' (ΔL=40nm) resonances: *x*, *y*, and *z* components of the M.

Section S5: Scattered powers of the λ₃' (Δ*L*=1nm), λ₄' (Δ*L*=40nm), and λ₃' (Δ*L*=40nm) resonances: *x*, *y*, and *z* components of the MT

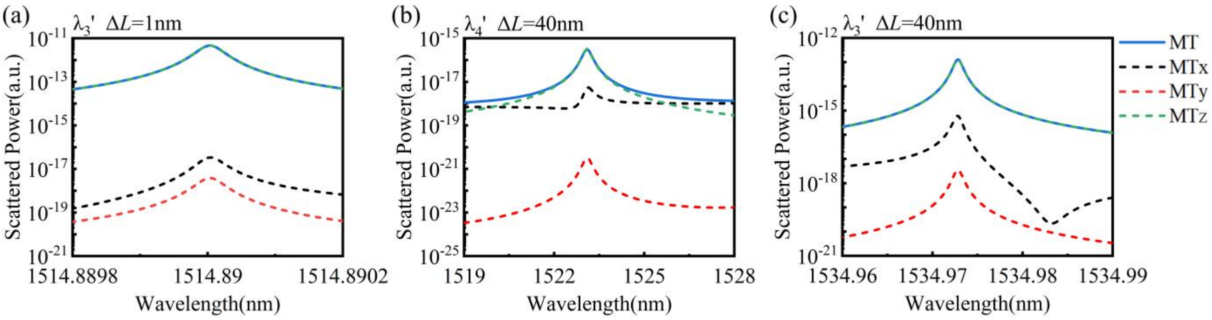

Figure S4. (a)-(b): Scattered powers of the λ_3' (ΔL=1nm), λ_4' (ΔL=40nm), and λ_3' (ΔL=40nm) resonances: *x*, *y*, and *z* components of the MT.

Section S6: Analysis of the related intrinsic band structures of TM and TE modes

To understand the physical origins of the excitation of quasi-BICs, the related intrinsic band structures of transverse magnetic (TM) and transverse electric (TE) modes from the metasurface are calculated for verification. Here, the cladding layers of the overlay and substrate in simulations are set to air to maintain the mirror symmetry in the *z*-direction.

From Figs. S5(a)-(b), it is evident that the dispersion curves of the two TM modes under consideration tend to intersect as they approach the Γ-point, resulting in an avoidance crossover phenomenon at the Γ-point due to the strong coupling effect. Similarly, the same is true for the two TE modes. The eigenmodes TE_1, TE_2, TM_1, and TM_2 exhibit infinite Q-factors at both Γ and off-Γ points. This indicates that TE_1, TE_2, TM_1, and TM_2 are typical BIC states. As depicted in Figs. S5(c)-(d), the electric field distributions of eigenmodes TE_1 and TE_2 at off-Γ points, and the magnetic field distributions of eigenmodes TM_1 and TM_2 at off-Γ points undergo a mode-swapping phenomenon attributed to the avoidance crossover effect. Additionally, the electric field distributions of TE_1 and TE_2 at off-Γ points align with the quasi-BIC resonance TR, while the magnetic field distributions of TM_1 and TM_2 at off-Γ points correspond to the quasi-BIC resonance MR. Consequently, the quasi-BIC resonance TR is the result of the joint action excitation of TE_1 and TE_2, while the quasi-BIC resonance MR is the result of the joint action excitation of TM_1 and TM_2.

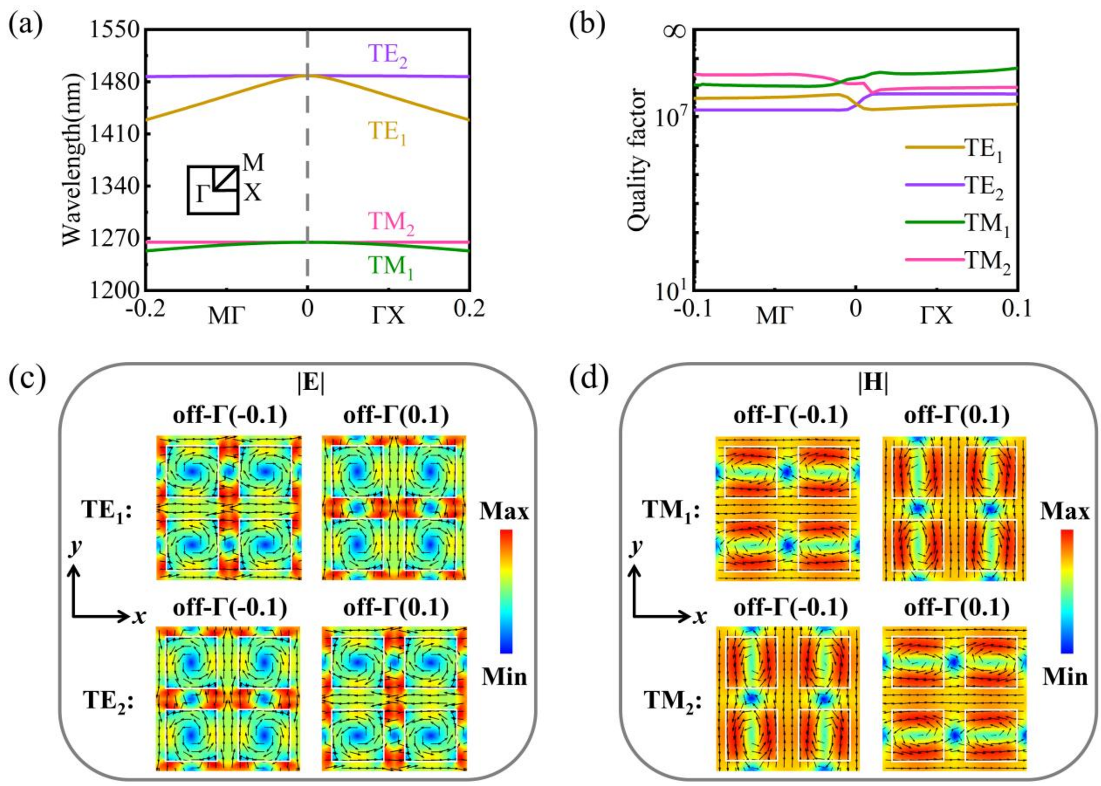

Figure S5. Analysis of the intrinsic band structures linked to the TE and TM modes corresponding to the quasi-BIC resonances: MR and TR. (a)-(b) Band structure and Q-factors of TE_1, TE_2, TM_1, and TM_2. (c) Electric field distributions of TE_1 and TE_2 in the *x*-*y* plane at off-Γ points. (d) Magnetic field distributions of TM_1 and TM_2 in the *x*-*y* plane at off-Γ points.

It is evident from Figs. S6(a)-(b) that the two dispersion curves, TE_3 and TE_4, will be close to each other as they approach the Γ point, exhibiting a tendency to intersect, resulting in an avoidance crossover phenomenon at the Γ-point due to the strong coupling effect. The eigenmodes TE_3 and TE_4 demonstrate infinite Q factors at the Γ point, which decrease notably as they move away from it. This indicates that TE_3 and TE_4 are typical BIC states. As depicted in Fig. S6(c), the magnetic field (H_z) distributions of eigenmodes TE_3 and TE_4 at Γ and off-Γ points, undergo a mode-swapping phenomenon attributed to the avoidance crossover effect. Additionally, magnetic field (H_z) distributions of TE_3 and TE_4 at Γ and off-Γ points align with the quasi-BIC resonances λ_1-λ_1' and λ_2-λ_2', indicating that these resonances arise from the excitation induced by TE_3 and TE_4.

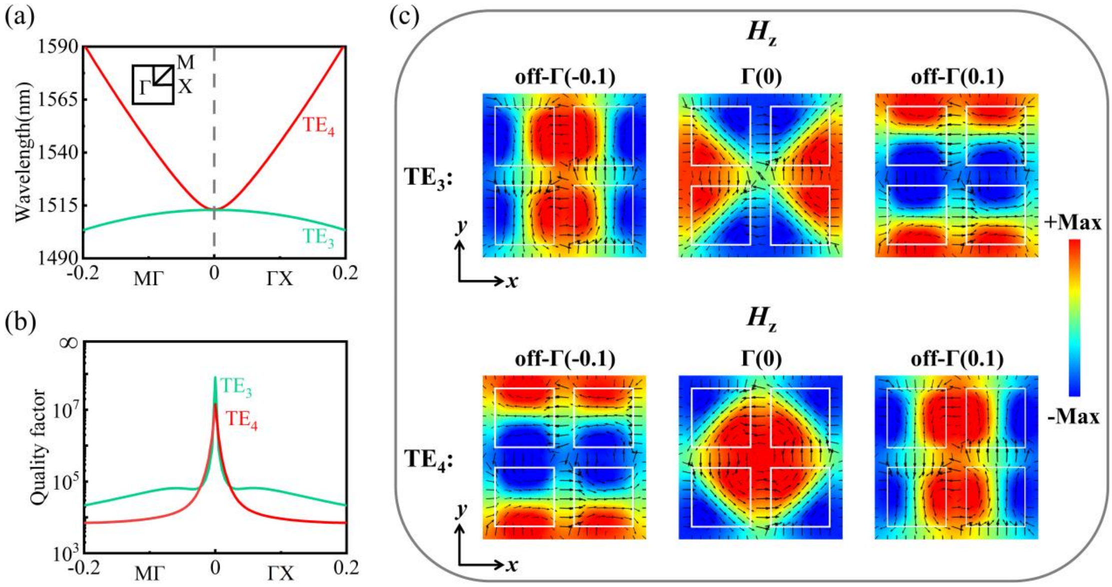

Figure S6. Analysis of the intrinsic band structures linked to the TE modes corresponding to the quasi-BIC resonances: λ_1-λ_1' and λ_2-λ_2'. (a)-(b) Band structure and Q-factors of TE_3 and TE_4. (c) Distributions of the *z*-component of the magnetic fields (H_z) in the *x*-*y* plane corresponding to TE_3 and TE_4 at Γ and off-Γ points.

Similarly, it is obvious from Figs. S7(a)-(b) that the dispersion curves of TM_3 and TM_4 will be close to each other as they approach the Γ point, exhibiting a tendency to intersect, resulting in an avoidance crossover phenomenon at the Γ-point due to the strong coupling effect. At the Γ point, eigenmodes TM_3 and TM_4 exhibit infinite Q-factors, which diminish significantly as they depart from this point. This indicates that TM_3 and TM_4 are typical BIC states. Illustrated in Fig. S7(c), the electric field (E_z) distributions of eigenmodes TE_3 and TE_4 at Γ and off-Γ points manifest mode swapping, a phenomenon attributed to the avoidance crossover effect. Furthermore, the electric field (E_z) distributions of TM_3 and TM_4 at Γ and off-Γ points align with the quasi-BIC resonances λ_3-λ_3' and λ_4-λ_4', indicating that these resonances originate from the excitation of TM_3 and TM_4.

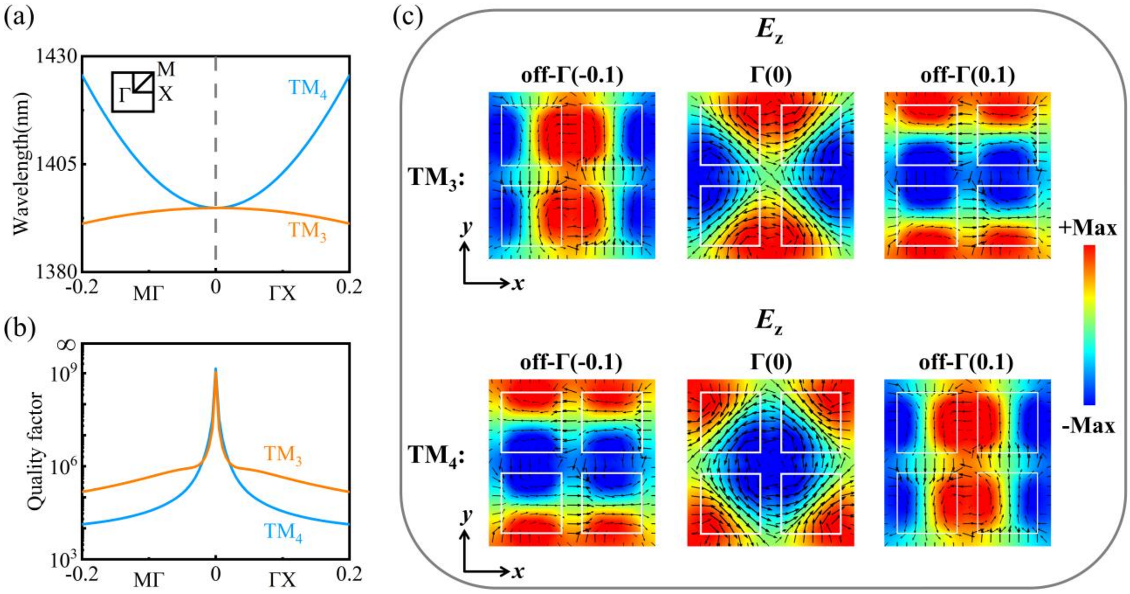

Figure S7. Analysis of the intrinsic band structures linked to the TM modes corresponding to the quasi-BIC resonances: λ_3-λ_3' and λ_4-λ_4'. (a)-(b) Band structure and Q-factors of TM_3 and TM_4. (c) Distributions of the *z*-component of the electric fields (E_z) in the *x*-*y* plane corresponding to TM_3 and TM_4 at Γ and off-Γ points.

Section S7: Analysis of the intrinsic band structure of TE mode associated with the new BIC state

We calculate the TE mode in the intrinsic band structures with only the upper and lower two square blocks on the left side of the unit cell, as shown in Fig. S8.

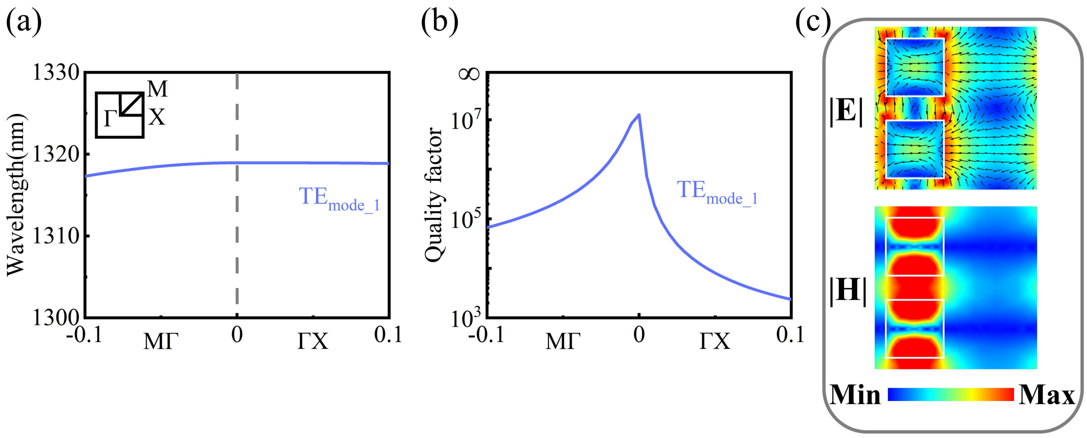

Figure S8. Analysis of the intrinsic band structures linked to the TE mode corresponding to the new BIC state. (a)-(b) Band structure and Q-factors of TE_{mode_1}. (c) Distributions of the electromagnetic field in the *x*-*y* plane corresponding to TE_{mode_1} at the Γ point.

Analysis of Figs. S8(a)-(b) reveals that TE_{mode_1} exhibits an infinite Q-factor at the Γ point, but its Q-factor decreases significantly when moving away from the Γ point. This indicates that TE_{mode_1} is a typical BIC state. Additionally, Figure S8(c) illustrates the corresponding electromagnetic field distributions of TE_{mode_1} at the Γ point, aligning closely with the quasi-BIC resonance λ_2 at ΔL = -350 nm.

Section S8: Analysis of the intrinsic band structure of TM mode associated with the new BIC state

Similarly, we computed the TM mode within the intrinsic band structure, assuming the right upper and lower two square blocks of the unit cell are coincident, with the length in the *y*-direction as Λ_y. Analysis of Figs. S9(a)-(b) reveals that TM_{mode_1} displays infinite Q-factors at both Γ and off-Γ points, indicating it is a typical BIC state. Additionally, Figure S9(c) illustrates the corresponding electromagnetic distributions of TM_{mode_1} at the Γ point, in agreement with the quasi-BIC resonance λ_3' at ΔL = 110 nm.

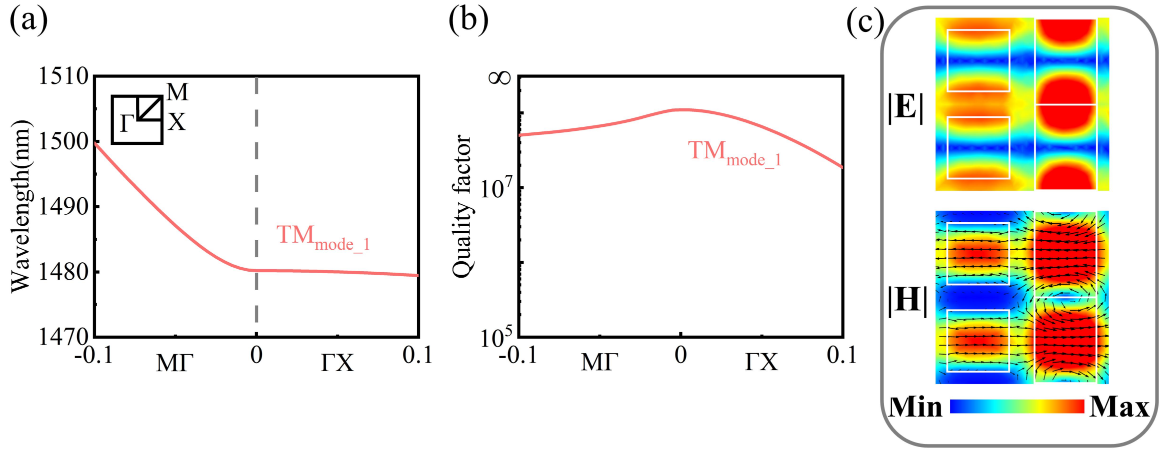

Figure S9. Analysis of the intrinsic band structures linked to the TM mode corresponding to the new BIC state. (a)-(b) Band structure and Q-factors of TM_{mode_1}. (c) Distributions of the Electromagnetic field in the *x*-*y* plane corresponding to TM_{mode_1} at the Γ point.

Section S9: Excitation of dual quasi-BIC resonances by length perturbation at E_x-polarised incidence

Figure S10(a) illustrates the transmission spectrum under E_x-polarized incidence, revealing the excitation not only of MR and TR but also of two novel leaky quasi-BIC resonance modes. These modes are designated as λ_3 and λ_4 for $\Delta L < 0$ nm, and λ_3' and λ_4' for $\Delta L > 0$ nm. The linewidths of λ_3-λ_4' and λ_4-λ_3' decrease as the absolute value of ΔL decreases. When ΔL = 0 nm, both λ_3-λ_4' and λ_4-λ_3' vanish, signifying no energy leakage from the bound state into the free-space continuum. Circles marked in Fig. S10(a) indicate that the radiative quality factor tends to infinity when ΔL = 0 nm, implying the presence of two BICs in the E_x-polarized incident light. Analyzing the transmission spectra within the range of ΔL from -60 nm to 60 nm also reveals evident avoidable crossover features at ΔL = 0 nm in the transmission spectra of λ_3-λ_4' and λ_4-λ_3'. The *x*-*y* plane electric field (E_z) distributions corresponding to λ_3-λ_4' and λ_4-λ_3' at various ΔL values demonstrate the hybridization behavior of the coupling process between the two BIC modes (see Fig. S10(b)). Moreover, the interconversion process between the two quasi-BIC resonance modes λ_3-λ_4' and λ_4-λ_3' is evident in Fig. S10b. Thus, the true counterpart of the quasi-BIC resonance λ_3 (ΔL < 0 nm) is λ_3' (ΔL > 0 nm), and similarly, the true counterpart of the quasi-BIC resonance λ_4 (ΔL < 0 nm) is λ_4' (ΔL > 0 nm). These analytical findings can be further corroborated by the TM modes in the intrinsic band structure (for details, see Figure S7 in section S6 of Supporting Information).

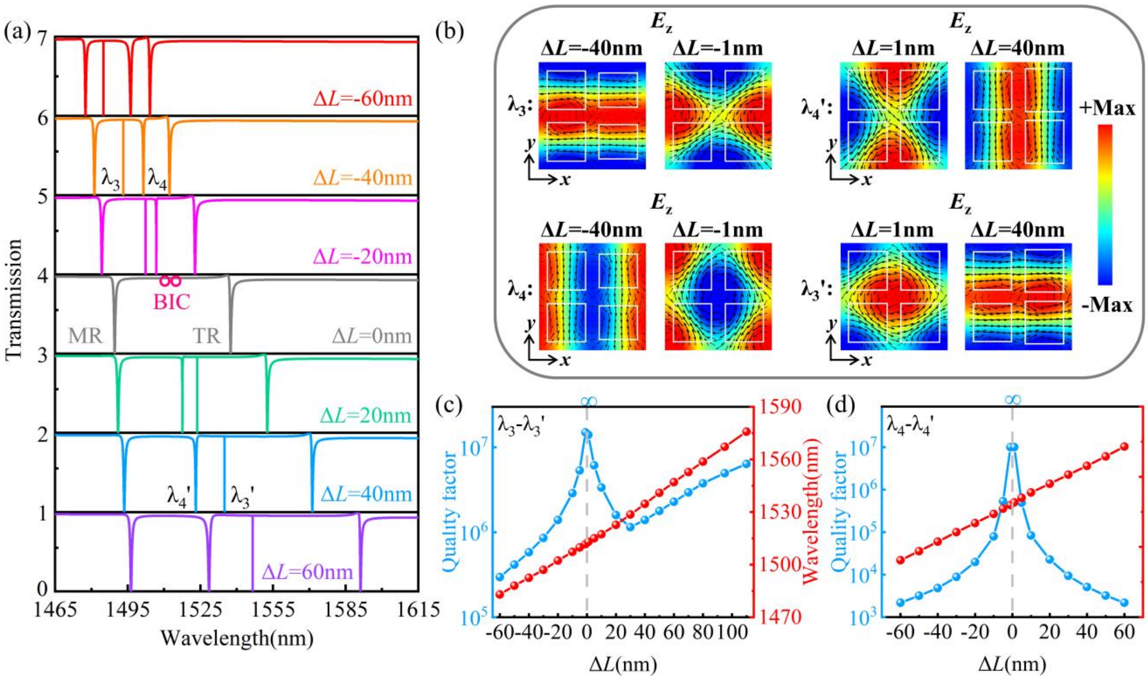

Figure S10. Optical properties of quasi-BICs: λ_1-λ_1' and λ_2-λ_2'. (a) Transmission spectra of the asymmetric metasurface ($\Delta L \neq 0$ nm) at E_x-polarised incidence. The remaining two resonance responses, excluding MR and TR, are denoted as λ_3 and λ_4 when ΔL < 0 nm, and as λ_3' and λ_4' when ΔL > 0 nm. (b) Distributions of the *z*-component of the electric fields (E_z) in the *x*-*y* plane for various ΔL values corresponding to the λ_3, λ_4, λ_3', and λ_4' resonances. Black arrows indicate the *x*-*y* plane magnetic field vector H_{xy}. (c)-(d) Resonance wavelengths and Q-factors of the λ_3-λ_3' and λ_4-λ_4'. resonances, respectively, versus the asymmetric parameter ΔL.

When varying the asymmetry parameter ΔL within the range of -60 to 60 nm, all four resonances exhibit monotonic redshifts. Specifically, Figs. S10(c)-(d) depict the resonance wavelengths (λ_3-λ_3' and λ_4-λ_4') as functions of the asymmetry parameter ΔL. Additionally, Figs. S10(c)-(d) illustrate the Q-factor of λ_3-λ_3' and λ_4-λ_4' concerning ΔL. At ΔL = 0 nm, the resonances of λ_3-λ_3' and λ_4-λ_4' vanish, and the Q-factor becomes infinite. For $\Delta L < 0$ nm and $\Delta L > 0$ nm, the peaks of the resonance Q-factors decrease significantly, indicating typical SP-BIC features. Surprisingly, the Q-factor corresponding to λ_3-λ_3' initially exhibits a decreasing trend as ΔL varies within the range of 0 to 110 nm (0 nm < ΔL < 30 nm). Subsequently, as ΔL varies between 30 and 110 nm, the Q-factor does not decrease but gradually increases. At ΔL = 110 nm (with a relative asymmetry parameter of 30.6%), the order of magnitude of the Q factor corresponding to λ_3-λ_3' remains above 10^6, decreasing by only one order of magnitude. The unexpected increase in the Q-factor is mainly attributed to the transition of the BIC mode state from the initial BIC state to the new BIC state (for details, see Figure S9 in section S8 and Figure S12 in section S9).

To enhance our comprehension of the fundamental physics underlying the excited quasi-BIC resonances, we analyze the corresponding electromagnetic near-field distributions of λ_3' (ΔL = 1 nm), λ_3' (ΔL = 40 nm), λ_4' (ΔL = 1 nm), and λ_4' (ΔL = 40 nm) at the resonant wavelengths, as depicted in Figs. S11(a)-(d). The electric field distributions of both λ_3' (ΔL = 1 nm) and λ_4' (ΔL = 1 nm) exhibit Qe modes. However, the magnetic field distributions demonstrate distinct mechanisms to generate the magnetic toroidal dipole (MT) moment between the square blocks. For λ_3' (ΔL = 1 nm), it can generate a single MT moment through the joint coupling of four square blocks within the unit cell. In contrast, λ_4' (ΔL = 1 nm) four simultaneous MT moments through the mutual coupling of square blocks between neighboring unit cells. Through analysis of the electromagnetic field distributions at λ_3' (ΔL = 40 nm) and λ_4' (ΔL = 40 nm), it is evident that the two MT moments induced by λ_3' (ΔL = 40 nm) are stimulated by the mutual coupling of the upper and lower square blocks within the unit cell on the left and right sides, respectively. In contrast, the two MT moments generated by λ_4' (ΔL = 40 nm) arise from the mutual coupling of the square blocks on the left and right sides within the unit cell, positioned on the upper and lower sides, respectively.

To better understand the role of dipole excitations in λ_3' (ΔL = 1 nm), λ_3' (ΔL = 40 nm), λ_4' (ΔL = 1 nm), and λ_4' (ΔL = 40 nm), we employ multipole decomposition calculations to determine the scattered powers contributions of the corresponding resonance multipoles, as depicted in Figs. S11(e)-(h). The results indicate that for λ_3' (ΔL = 1 nm), the dominant multipole is MT, exhibiting the highest scattered power. It is followed by Qe, P, and Qm. Conversely, for λ_3' (ΔL = 1 nm), Qe takes precedence, followed by Qm and MT. For λ_1' and λ_2' at ΔL = 40 nm, MT dominates in both instances, with Qe and Qm following. Analysis of the *x*, *y*, and *z* components of the MT scattered power reveals that the *z* component exhibits the highest intensity in λ₃' (Δ*L* = 1 nm), λ₃' (Δ*L* = 40 nm), and λ₄' (Δ*L* = 40 nm) (for details, see Figure S4 in section S5). In summary, the silicon square block array induces dual quasi-BIC resonances, λ_3-λ_3' and λ_4-λ_4', when subjected to length perturbation under E_x-polarized light. These resonances arise from MT-dominated quasi-SP-BICs when Δ*L* deviates from 0. Conversely, as Δ*L* approaches 0, the strong coupling effect, attributed to the avoidable crossover property, resulting in the generation of resonant modes dominated by MT and Qe quasi-F-W-BICs.

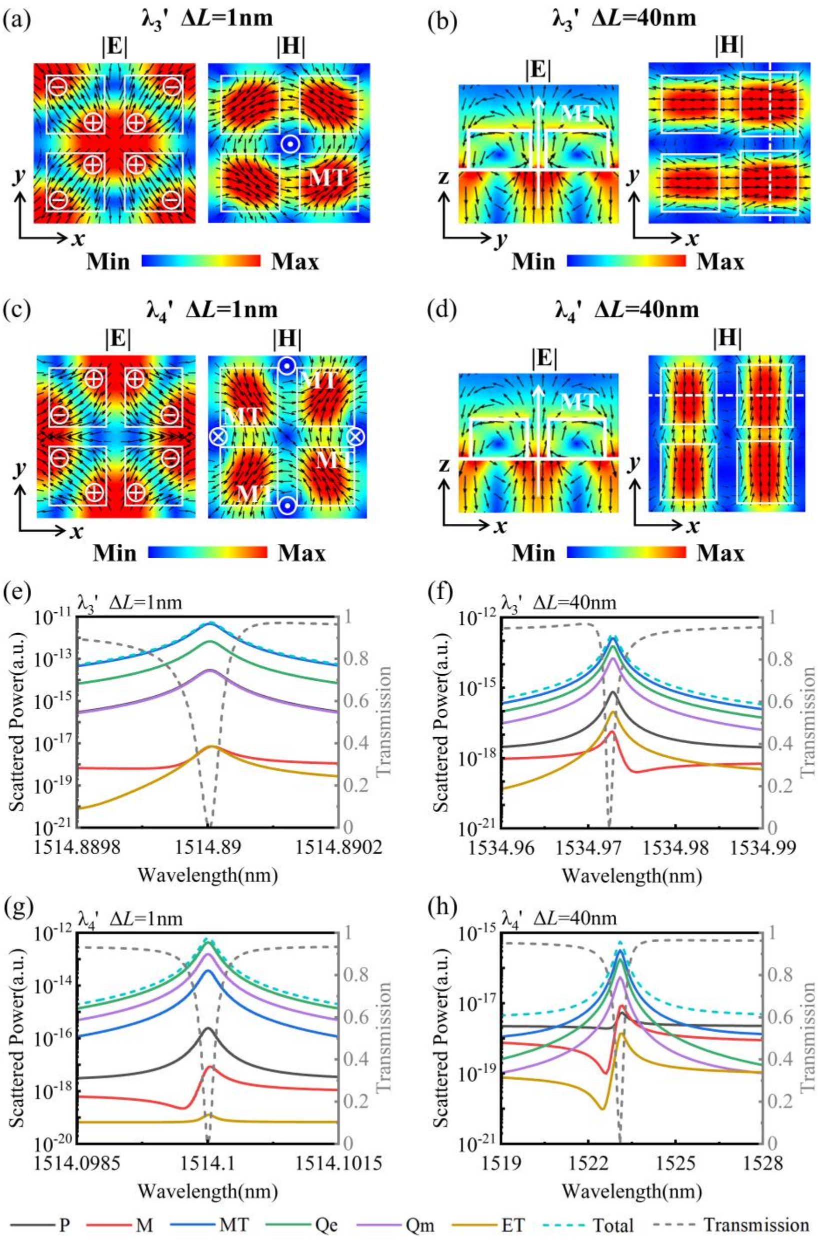

Figure S11. Electromagnetic-field distributions and demonstration of the role of dipole excitation in quasi-BICs: λ_3' and λ_4'. (a)-(d) Electromagnetic-field distributions of the λ_3' (Δ*L* = 1 nm), λ_3' (Δ*L* = 40 nm), λ_4' (Δ*L* = 1 nm), and λ_4' (Δ*L* = 40 nm) resonances, respectively.

Black arrows indicate the displacement current vector and magnetic-field vector, respectively. (e)-(h) Scattered powers of the λ_3' (ΔL = 1 nm), λ_3' (ΔL = 40 nm), λ_4' (ΔL = 1 nm), and λ_4' (ΔL = 40 nm) resonances, respectively.

We analyzed the alterations in the electromagnetic field distributions of the quasi-BIC resonant mode λ_3' within the x-y plane as ΔL ranges from 50 nm to 110 nm, as shown in Fig. S12. At ΔL = 110 nm, it corresponds to the upper and lower two square blocks on the right side nearing coincidence in the *y*-direction, with the length in the *y*-direction approximating Λ_y. At this time, we computed the TM mode within the intrinsic band structure, assuming the right upper and lower two square blocks are coincident, with the length in the *y*-direction as Λ_y (for details, see Figure S9 in section S8). We noted that the calculated electromagnetic field distributions of the TM mode align with that at ΔL = 110 nm. The variation in its Q-factor indicates a typical BIC mode, precisely explaining the change in the Q-factor associated with the quasi-BIC resonance λ_3' that first decreases and then increases when ΔL varies from 0 nm to 110 nm.

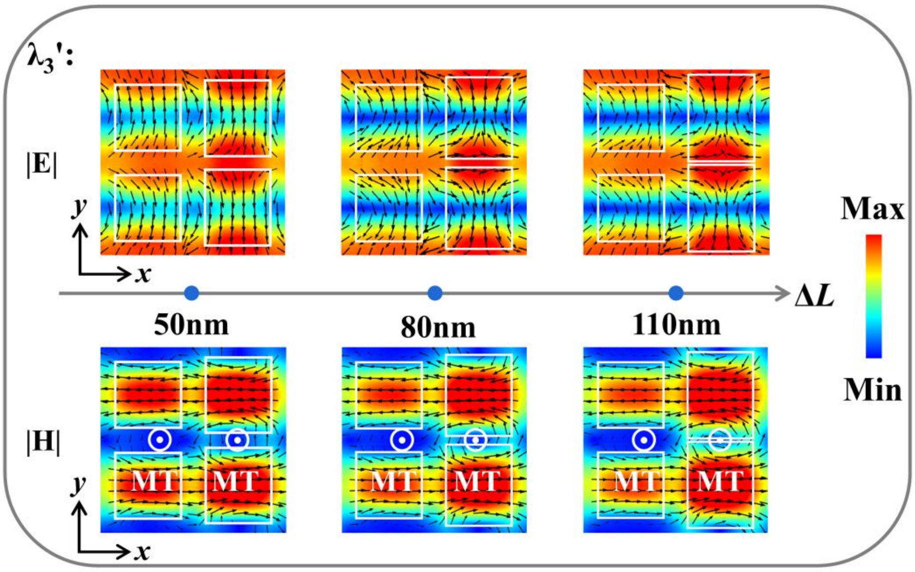

Figure S12. Variation of the electromagnetic field distributions in the *x*-*y* plane within the quasi-BIC resonant mode λ_3' while varying ΔL from 50 nm to 110 nm.

Section S10: Transmission spectra of the asymmetric metasurface concerning different geometric parameters at E_y-polarised incidence

We calculated the transmission spectra of the asymmetric metasurface structure (ΔL = 40nm) at E_y-polarised incidence under various geometrical conditions to investigate the relationship between the quasi-BIC resonances and different geometrical parameters, as illustrated in Fig.

S13. All other geometrical parameters remain consistent with those presented in Fig. 3(a) of the main text, with only the variable parameters being altered, as indicated in each figure.

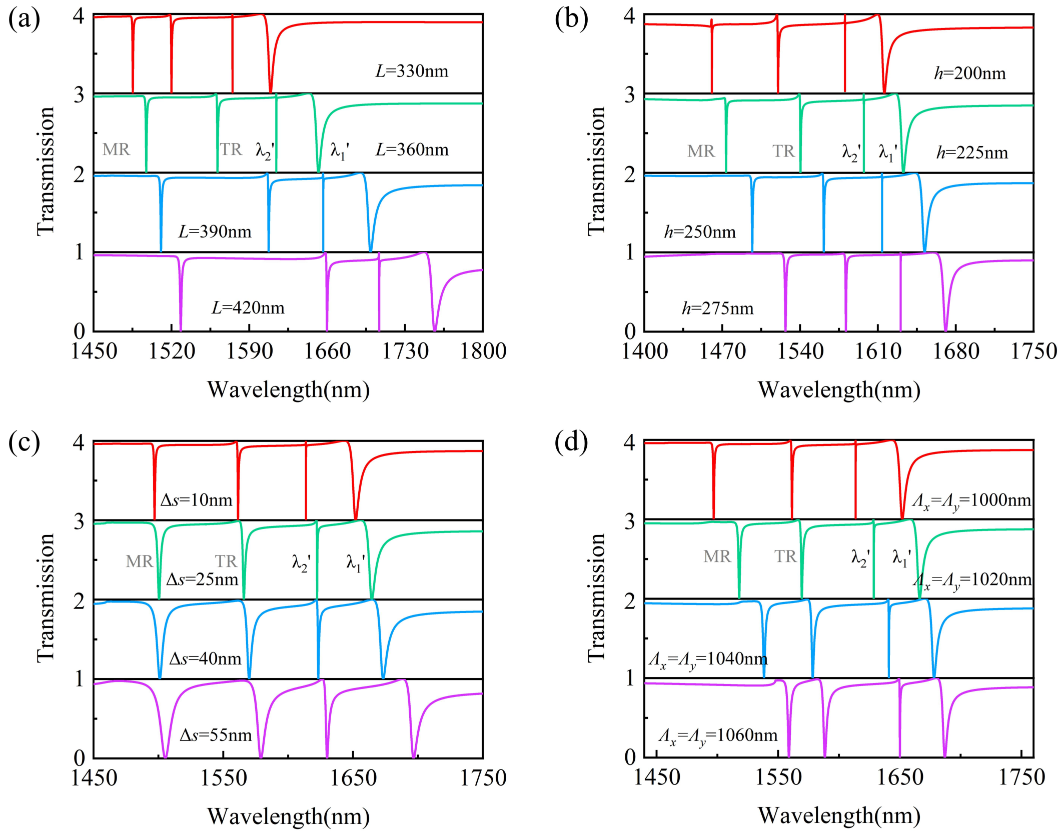

Figure S13. Transmission spectra of the asymmetric metasurface structure (ΔL = 40 nm) with different (a) L, (b) h, (c) Δs, and (d) Λ_x and Λ_y at E_y-polarised incidence.

Section S11: Influence of loss in silicon on Q-factor of quasi-BIC at E_y-polarised incidence

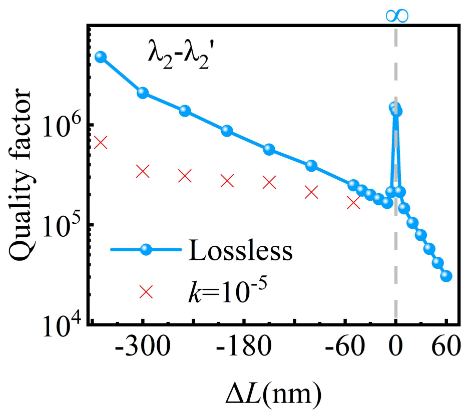

Figure S14. Q-factors of the λ_2-λ_2' resonance concerning ΔL (−350 nm to 60 nm) for lossless and lossy high Q metasurfaces.

The effect of losses is quantified by adding an imaginary part k to the Si refractive index and shown in Fig. S14. When k=10^{-5}, the Q-factor of the λ_2-λ_2' resonance can remain above 10^5 as the asymmetry parameter ΔL varies from -350 nm to -50 nm.

Section S12: Sample fabrication process

In this section, we provide a brief overview of the sample fabrication process: Silicon dioxide (SiO_2)-based samples can be produced using silicon-on-insulator (SOI) wafers. The fabrication process primarily involves electron beam lithography (EBL) and inductively coupled plasma (ICP) etching techniques. First, ZEP520A is spin-coated onto a clean SOI wafer to serve as the resist layer. Subsequently, the desired pattern is drawn on the resist layer using an EBL tool. After careful development and fixation, the pattern is transferred to the silicon diaphragm via the ICP reactive ion etching (ICP-RIE) technique, employing an SF_6/C_4F_8 mixture. Finally, the residual resist is immersed in N-methyl-2-pyrrolidone (NMP) and removed using ultrasound.

Section S13: Scaling to other spectral ranges

We scaled the structural parameters of the metasurface as follows: $\Lambda_x = \Lambda_y$ = 500 nm, L = 160 nm, h = 160 nm, s = 50 nm. The simulated transmission spectra presented in Fig. S15(a) and the Q-factor variations of the quasi-BIC resonance $QBIC_2$ depicted in Fig. S15(b) show results similar to those in Figs. 3(a) and (d) of the main text, thereby confirming their scalability at visible wavelengths.

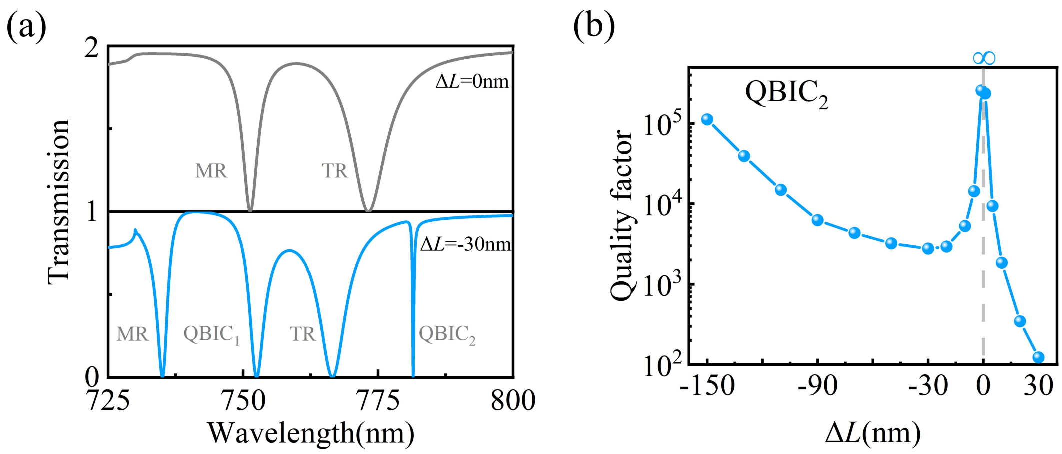

Figure S15. (a) Transmission spectra of symmetric metasurfaces (ΔL= 0 nm) and asymmetric metasurfaces (ΔL= -30 nm) at E_y-polarised incidence. (b) Q-factor of the $QBIC_2$ resonance concerning ΔL (−150 nm to 30 nm).

References

1. S. Fan, "Sharp asymmetric line shapes in side-coupled waveguide-cavity systems," Appl. Phys. Lett. **80,** 908 (2002).
2. B. Luk'Yanchuk, N. I. Zheludev, S. A. Maier, *et al*., "The Fano resonance in plasmonic nanostructures and metamaterials," Nat. Mater. **9,** 707 (2010).
3. E. Radescu and G. Vaman, "Exact calculation of the angular momentum loss, recoil force, and radiation intensity for an arbitrary source in terms of electric, magnetic, and toroid multipoles," Phys. Rev. E **65,** 046609 (2002).
4. V. Savinov, V. Fedotov, and N. I. Zheludev, "Toroidal dipolar excitation and macroscopic electromagnetic properties of metamaterials," Phys. Rev. B **89,** 205112 (2014).
5. A. A. Basharin, M. Kafesaki, E. N. Economou, *et al*., "Dielectric metamaterials with toroidal dipolar response," Phys. Rev. X **5,** 011036 (2015).
6. S. Li and K. B. Crozier, "Origin of the anapole condition as revealed by a simple expansion beyond the toroidal multipole," Phys. Rev. B **97,** 245423 (2018).
7. H. Liu, H. Luo, C. Chen, *et al*., "Excitation of electric toroidal dipole resonance and design of chiral materials," Opt. Laser Technol. **157,** 108643 (2023).